City Research Online

City, University of London Institutional Repository

Citation: Fostiropoulos, S., Strotos, G., Nikolopoulos, N. & Gavaises, M. (2020). Numerical investigation of heavy fuel oil droplet breakup enhancement with water emulsions. Fuel, 278, 118381. doi: 10.1016/j.fuel.2020.118381

Numerical investigation of Heavy Fuel Oil droplet breakup enhancement with water emulsions

Stavros Fostiropoulos*[1,2], George Strotos[3], Nikolaos Nikolopoulos[1] and Manolis Gavaises[2]
[1]Centre for Research and Technology Hellas/Chemical Process and Energy Resources Institute (CERTH/CPERI), Egialeias 52, Marousi, Greece
[2]City University of London, School of Engineering and Mathematical Sciences, Northampton Square, EC1biliV 0HB London, UK
[3]University of Thessaly, 41110 Larissa, Greece
*Corresponding author: fostiropoulos@certh.gr

Abstract

The heating and explosive boiling leading to fragmentation of immiscible heavy fuel oil-water droplets, termed as W/HFO emulsions, is predicted numerically by solving the incompressible Navier-Stokes and energy equations alongside with a set of three VoF transport equations separating the interface of co-existing HFO, water liquid and water vapour fluid phases. Model predictions suggest that explosive boiling of the water inside the surrounding HFO, ought to their different boiling points, accelerates droplet breakup; this process is termed as either puffing or micro-explosion. In contrast to past studies which predefine the presence of vapor bubbles inside the water droplet, this is predicted here with a phenomenological model based on local temperature and superheat degree. Following their formation, the growth rate of the bubbles is computed with OCASIMAT phase-change algorithm. Moreover, the fuel droplet is simultaneously subjected to convective air flow which further contributes to its deformation. As a result, the performed simulations quantify the relative time scales of the aerodynamic-induced and the emulsion-induced breakup mechanisms. The conditions examined refer to a highly viscous emulsified heavy fuel oil droplet in a gas phase having fixed temperature and pressure equal to 1000 K and 30 bar, respectively. Initially, a benchmark case demonstrates the detailed mechanisms taking place, concluding that droplet fragmentation occurs only at a part of the fuel-air interface, resembling characteristics similar to puffing. Next, a parametric study with Weber number ($Oh = 0.9, We < 200$) shows that puffing process can speed up to 10 times the breakup of the droplet relative to aerodynamic breakup.

Keywords: CFD, fuel oil-water emulsion, breakup, VoF, vapor nucleation, boiling

Nomenclature

Roman symbols		***Subscripts***	
a	Thermal diffusivity [m^{2}s^{-1}]	∞	far-field quantity
A	Interfacial surface area [m^2]	0	initial value
b	Scriven bubble growth factor	b	bubble
c_p	isobaric heat capacity [J kg^{-1} K^{-1}]	br	breakup
d	Distance [m]	c	critical

D	Diameter [m]
E	Energy [J]
f	Physical variable
h_{lv}	heat of vaporization [J kg^{-1}]
k	thermal conductivity [W m^{-1} K^{-1}]
m	mass [kg]
Oh	Ohnesorge number
p	pressure [Pa]
Pe	Peclet number
R	radius [m]
Re	Reynolds number
St	Stefan number
t	time
T	temperature [K]
u	Velocity [ms^{-1}]
V	Volume [m^3]
We	Weber number

Greek symbols

α	Volume fraction
ΔT_s	Superheat degree [K]
μ	Dynamic viscosity [Pa s]
ρ	density [kg m^{-3}]
σ	Surface tension [N m^{-1}]

CFD	values provided by CFD
dr	water sub-droplet
g	gas
i	interface
l	liquid
m	mass-averaged
oil	Oil phase/droplet
q	phase number
s	surface
sat	saturated
sh	Shear
v	Vapor
w	water

Dotted symbols

$\dot{\varphi}$	first time derivative
$\ddot{\varphi}$	second time derivative

1. Introduction

Across the world, and despite the increasing fraction of electric vehicles (EVs) (they are expected to reach 60% in passenger car and light duty vehicles and up to 15% for heavy duty over the next two decades [1, 2] the forecasted increase of liquid fossil fuel usage will be 25% globally and more than 50% for heavy-duty vehicles over the same time period; this is due to the constantly increasing global energy needs, urbanisation and population growth [3]. Diesel engines are massively used as a source of power, especially for transportation, due to their relatively high power output and fuel economy [4]; however, electrification in this transport/power sector is expected to be a long-term process. Combustion products from Diesel engines, especially, NO_x and particulate matter (PM), are known to be harmful to both the environment and directly to human health when inhaled. According to [5], anthropogenic emissions contribute more than 90% to the climate change while Diesel engines are responsible for ~2/3 of the total liquid fossil fuel utilization globally. Besides the environmental impact, lung cancer, asthma and cardiovascular diseases are linked to such emissions. The aforementioned concerns have triggered many research efforts investigating mechanisms for reducing the in-cylinder formed pollutants in heavy duty and marine Diesel engines [6, 7]; among them, water emulsions into heavy fuels is known to offer significant simultaneous reduction in NOx and PM emissions [8].

Water can be introduced to the engine by three common methods: (i) emulsified fuel-water in Diesel emulsion (WiDE); (ii) in-cylinder water injection [9]; and (iii) water injection into the intake air (fumigation) [10]. In both fumigation and direct water injection, water is in direct contact with the fuel injection system and the piston cylinder which may cause oil contamination and corrosion issues. Thus, the most promising approach to utilise water for reduction of emissions is considered to be the WiDE method [11, 12]. The fact that no engine modification is required, points out water-emulsified fuels as a cost-effective solution. On the other hand, both fumigation and direct water injection demand engine modification, which has high additional cost [13].

Emulsion is generated by means of mechanical agitation in the presence of surface active agents, called surfactants or emulsifiers. The latter are needed in order to avoid the coalescence of the water sub-droplets. When an emulsified droplet is injected inside a combustion chamber, heat is transferred from the hot ambient air to the emulsified droplet. The host (parent) droplet has higher boiling point than the corresponding one of the water sub-droplet; the water sub-droplet becomes superheated and eventually boils (Figure 1). The water droplet is contained in a uniform substance (oil droplet) free of nucleation sites and for that reason it is capable of exceeding its boiling point and experiences a metastable regime. At some point though, as the droplet heats up and the local temperature exceeds the boiling point of water, homogeneous nucleation occurs (in contrast to heterogeneous boiling which occurs when a fluid is in contact with solid surfaces) and water starts to boil [14]. Vapor generation leads to expansion and deformation of the surrounding oil droplet and eventually leads to its fragmentation. Micro-explosion is defined as the process during which complete breakup of the oil droplet occurs, while if just a portion of the oil droplet is ruptured, the process is termed as puffing. The aforementioned breakup regimes have been widely discussed in the literature, see selectively [12, 15, 16].

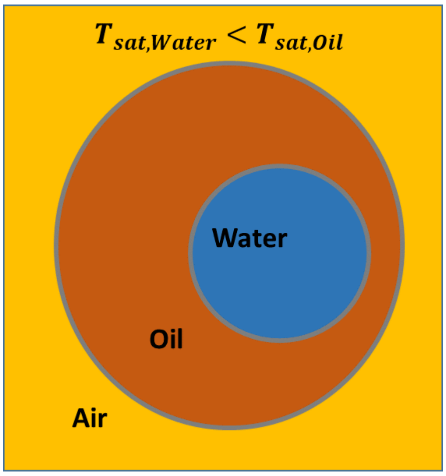

Figure 1. Emulsion droplet indicative configuration

Despite the potential benefit of using emulsified fuels, the detailed physical mechanisms that occur during micro-explosion and puffing are not clear. In the experimental work of [17], homogeneous explosive boiling of a vapor bubble inside a superheated water droplet has been studied and the size of the vapor bubble during its growth was measured. In a similar experiment by [18], it was observed that during explosive boiling, liquid particles were torn from the liquid-gas interface, alongside with bubble oscillations. So far, the majority of experiments on emulsion droplets has focused on the combustion characteristics after the puffing/micro-explosion induced secondary atomisation [19-21]; thus, the overall dynamics of a single droplet cannot be revealed. In single droplet experiments, a relative large droplet (O (1 mm)) compared to those realized in engines has been investigated. In the work of [22] it was found that the water volume fraction and the quantity of surfactant may influence the tendency towards micro-explosion. The latter can also be affected by the size distribution of the dispersed water sub-droplets [23]. Recently, single droplet experiments having sizes similar to those realised in diesel engines (O (10 μm)), were performed by [24, 25]. In the experiment of [25], the effect of water content on the characteristics of micro-explosion was investigated, using a high speed video camera. However, the physical processes taking place inside the emulsion and during the growth rate of the boiling water have not been revealed.

The factors that influence the growth rates of boiling bubbles in pool liquids have been extensively studied over the last 50 years. In general, density fluctuations and disturbances are always present in liquids and are responsible for the formation of bubble nuclei. Nano or sub-μm vapor bubble nuclei collapse and disappear due to Laplace pressure in an accelerated manner; however, some of them may pass a critical radius ($R_0 = 2\sigma/\Delta P_0$) and continue to grow. The aforementioned expression must be couched in terms of the probability that a bubble with R_0 will occur at the time where a critical pressure difference ΔP_0 is applied. According to [26], liquids are able to withstand pressure differences of $3 \cdot 10^4$ to $3 \cdot 10^5$ bar, which correspond to a critical bubble radius comparable to the intermolecular distance (10^{-10}m). Since the vapor bubble has passed its critical radius, it continues growing in three different phases. The first growth phase is surface tension dominated where the pressure difference is balanced by the surface tension, while the bubble has the same temperature as the surrounding liquid. That regime diminishes quickly as the bubble size increases. Next, the bubble growth is limited by the inertia of the surrounding liquid and the bubble radius is a linear function of time. The bubble continues expanding, while its surface temperature decreases due to evaporation. The internal bubble pressure decreases until the driving force due to pressure difference is negligible. The final phase of growth is “diffusion” controlled, where bubble surface temperature will reach the bulk saturation temperature, and the growth is limited by heat diffusion. At this regime, the growth rate of bubble decreases substantially; the bubble radius R increases with $\sqrt{t}$ instead of t. Theoretical models have been developed in the past that accurately predict vapor bubble growth in either inertial [27] or diffusive [28-31] regime. In the work of [32], a solution is obtained that combines the works of [27] and [29] and manages to predict successfully the bubble growth rate in both inertial and diffusion dominated regimes. According to this study, the critical radius (eq. 1) that defines the transition from the inertial to the diffusion-controlled regime is determined by the fluid properties and the liquid superheat:

$$R_c = 2\sigma T_{sat}/h_{lv}\rho_v \Delta T_s \tag{1}$$

The latter size is significant for the development of the current CFD model, since the initial bubble size in the simulations is assumed to be diffusion-controlled in order to be capable to resolve it.

The development of micro-explosion models could shed light on the relevant processes. One of the first emulsion mathematical models is that of [33], which predicts the vapor bubble growth ought to homogeneous nucleation within a liquid water droplet. However, puffing/micro-explosion phenomenon was not taken into account. A similar approach was followed by [34], who employed Rayleigh’s model to predict vapor bubble growth in the centre of a liquid water droplet; however, the assumptions made in that model (e.g. the droplet is stationary) may not be suitable for engine fuel spray conditions. Simplified mathematical models which can be useful for engineering applications have also been suggested [35, 36], but they cannot provide details of the physical processes during deformation and breakup of emulsion droplets. Finally, advanced CFD models proposed recently by [15, 16] gave insight on the underlying physics of micro-explosion and puffing. In the work of [15], simulations of a static emulsion droplet have been performed where the latter is considered to be preheated in the boiling temperature of its embedded water sub-droplet. Besides the predefined temperature, the location and size of the vapor bubble were also predefined. Convective heating of emulsion droplets has been studied in [16]; the model predictions indicated that the boiling of the embedded water sub-droplet highly depends on the liquid Peclet number and the internal circulation inside the parent droplet.

Droplet secondary breakup due to aerodynamic forces is typically characterized by the Weber (We) and Ohnesorge (Oh) numbers (i.e it is controlled by inertia, surface tension and viscous forces), as also by the Reynolds number and the liquid to gas density (ε) and viscosity (N) ratios [37], which play a secondary role. Breakup results in droplet fragmentation into several smaller droplets and requires a finite time of the order of the shear breakup timescale ($t_{sh} = D\sqrt{\varepsilon}/u$) [38] to be completed. For the case of emulsified droplets, a crucial question arises: is there enough time for the droplet to heat-up, nucleation sites to appear and explosive boiling to occur, when the former is subjected to aerodynamic forcing? To the best of our knowledge, the aforementioned physical processes have only been addressed independently, with the aid of simplified mathematical models [33, 36, 39, 40].

The aim of the present study is to clarify this question; from a physical standpoint, the current work addresses the combined effect of thermal (due to micro-explosion) and aerodynamic secondary droplet breakup processes, with the aid of a CFD model capable of simulating the overall phenomenon, starting from convective heating of the emulsion droplet up to puffing/micro-explosion. The model considers vapor generation and edge regression of W/HFO interface and captures the puffing/micro-explosion-induced droplet fragmentation. Moreover, and unlike previous studies, the vapor nucleation sites are not predefined, but they are predicted as part of the solution, based on the local liquid temperature. The examined properties are similar to that of a highly viscous HFO, which is typically used in large marine Diesel engines. HFO is treated here as single component, thus species distribution inside the parent droplet is not considered. As aforementioned, homogeneous nucleation occurs when a tiny vapor nucleus is generated inside a uniform liquid. Emulsion experiments have shown that the probability of vapor nucleation is related to the temperature of the liquid, while the vapor nuclei are generated close to the water interface [41, 42]. Since it is difficult to resolve the vapor nucleation phenomenon, a mechanistic algorithm that accounts for the initial formation of a small vapor bubble and takes into account the aforementioned experimental findings, has been developed and implemented into the CFD code.

In the following section the mathematical description of the emulsion droplet breakup model is provided, alongside with the vapor bubble formation algorithm and the OCASIMAT phase-change model for vapor bubble growth [43]. Examined cases and results are following, while the most important conclusions are summarized in the end.

2. Numerical model and methodology

2.1 Volume of Fluid method

The numerical technique that is used in this study for tracking the interface between multiple fluids/phases is the Volume of Fluid method [44]. The VoF method solves a single set of momentum equations and identifies each fluid by a volume fraction denoted by a. Specifically, in the emulsion model three phases initially exist (Air, Oil, Water) and at some point during the simulation an additional phase is solved due to sudden appearance of vapor. The volume fraction a is defined as the percentage of volume covered by each phase in the computational cell with respect to the total volume of the cell. In each cell the sum of the volume fractions of all phases must be equal to unity. Mathematically, when volume fraction of phase q inside a cell is unity, the cell is completely covered by the material of phase q, while when the volume fraction is equal to zero, the cell is empty of phase q. Finally, when the volume fraction of q^{th} fluid is between 0 and 1, the cell contains the interface between the q^{th} fluid and one or more other fluids. Upon the volume fraction value of phase q, variables and properties represent volume-averaged values of phase q. For instance, the physical variable f within a computational cell will be computed as follows:

$$f = \sum_{q=1}^{N} a_q\, f_q, \text{ where } N = \text{number of phases} \tag{2}$$

The advection equation for the volume fraction is defined as:

$$\frac{\partial a_q}{\partial t} + \nabla \cdot \left(\overrightarrow{u_q} a_q\right) = \frac{\dot{m}_{pq}}{\rho} \nabla a_q \tag{3}$$

where the term in the RHS stands for any additional volumetric mass source term.

A single momentum equation is solved throughout the entire numerical domain, and the computed velocity field is shared among all the phases. The momentum equation is dependent on the properties of density ρ and dynamic viscosity μ, which are computed according to Eq. 2, and it is written in the form:

$$\frac{\partial(\rho \vec{u})}{\partial t} + \nabla \cdot \left(\rho \vec{u} \otimes \vec{u} - \vec{T}\right) = \rho \vec{g} - \vec{f}_\sigma \tag{4}$$

where $\vec{T}$ is the stress tensor and $\vec{v}$ is the velocity. Surface tension term denoted as $\vec{f}_\sigma$ is taken from [45] and for the case that only two phases are present inside a computational cell, the relation reads:

$$\vec{f}_\sigma = \sigma_{pq} \frac{\rho \kappa_p \nabla a_p}{\frac{1}{2}(\rho_p + \rho_q)} \tag{5}$$

where k is the curvature of the free surface, approximated as the divergence of unit surface normal “n”, and reads:

$$\kappa_p = \nabla \cdot \hat{n} \tag{6}$$

$$\hat{n} = \frac{\nabla a_p}{\left|\nabla a_q\right|} \tag{7}$$

The energy equation, which is also shared among the contributing phases, is presented in Eq.8, where energy E is a mass-averaged variable between each additional phase:

$$\frac{\partial(\rho E)}{\partial t} + \nabla \cdot \left(\vec{u}(\rho E + p)\right) = \nabla \cdot \left(k_{eff} \nabla T\right) + S_h \tag{8}$$

$$E = \frac{\sum_{q=1}^{n} \alpha_q \rho_q E_q}{\sum_{q=1}^{n} \alpha_q \rho_q} \tag{9}$$

In the equations above, density ρ and effective thermal conductivity, denoted by k_{eff}, are shared among the phases. Finally, S_h contains contributions from any volumetric heat sources existed in the model. The solution methods selected alongside with the numerical details are provided in the following sections.

2.2 Vapor bubble formation and growth

As nucleation theories aiming to resolve formation of vapor nuclei inside the bulk of the water are out of scope of the present work, a conceptual approach for vapor bubble formation is developed and implemented in the CFD model. The criteria under which a vapor bubble is generated are the following. First, the formation site, which is a computational cell (Figure 2; left panel), should be located at a specific distance (d_i) from the oil-water interface [18]. This distance has a finite length preventing contact of the bubble with the oil-water interface (Figure 2; Right panel). In case that vapor, water and oil phases coincide in a computational cell, numerical issues arise. A relevant parametric study with bubble's surface depth is presented in Appendix A, proving that the obtained results are not sensitive to this numerical selection. Next, the superheat degree (ΔT_s) of vapor generation is also an input parameter of the model. The algorithm checks if the selected superheat degree has been reached in the aforementioned computational cell. Different superheat values from 5 to 25 K have been examined but the results seem not to be sensitive (Appendix A). Once the aforementioned criteria are fulfilled in a computational cell, a bubble is formed at the center of the computational cell. As discussed in the literature, the vapor bubble should reach a critical size ($R_0 = 2\sigma/\Delta P_0$) in order to start growing and not collapsing immediately due to surface tension. The first growth phase is inertia-controlled, which ends quickly (typically ∽0.1 μs) and diffusion-controlled growth follows. The transition to the diffusive regime is characterized by a critical bubble radius [32], which depends on fluid properties and liquid superheat. In the examined cases of the current study that radius was computed to be of the order of 0.11 μm (eq. 1). As it's computationally expensive to resolve such a length scale, the vapor bubble is initiated with a finite radius size ($R_{b,0} = 0.25$ μm). It should be noted that the influence of the initial bubble radius on the obtained results has been checked by performing numerical experiments, pointing out that the breakup process is identical and only the early development of the bubble differs; similar behavior has been observed also in the work of [15]. Since the initial bubble starts growing due to heat diffusion, as it is larger than

R_c, a bulk saturation temperature value is imposed at its interface (506 K), while its internal pressure is defined by the surface tension term ($2\sigma/R_{b,0}$). The latter is calculated to be 2 bar. A schematic configuration of vapor bubble formation is illustrated in Figure 2.

Summarizing, the criteria for bubble creation in a computational cell are the following: i) $T_{cell} \geq T_{sat} + \Delta T_s$, ii) d_i to be the smallest possible, without vapor water and oil coexisting in a computational cell (in the current resolution $R_{b,0} = 0.25$ μm as already mentioned).

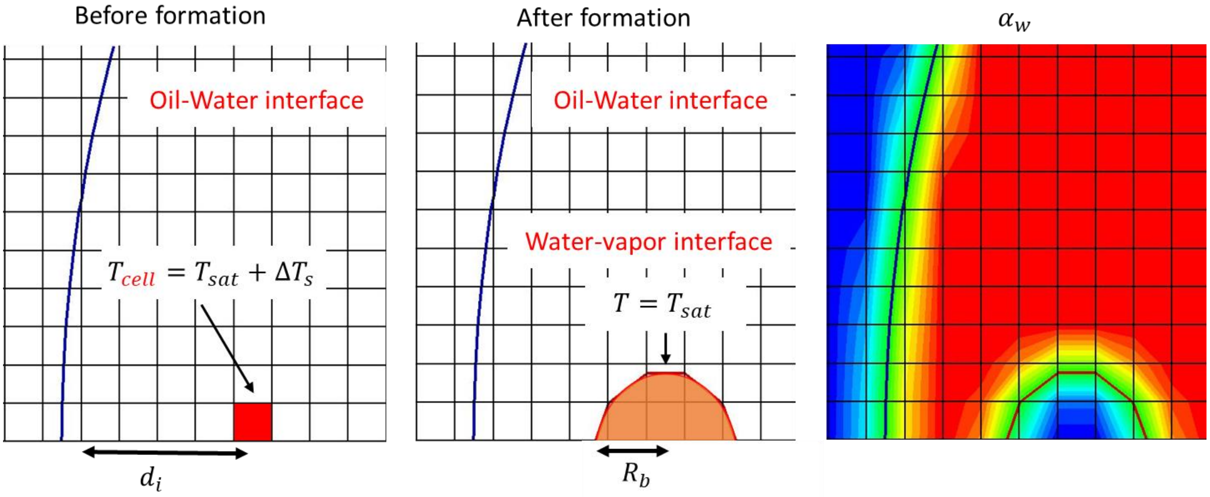

Figure 2. Configuration of vapor bubble formation

Right after its formation, the vapor bubble starts growing due to interfacial heat and mass transfer. A method termed as OCASIMAT [43] is implemented in the CFD model and calculates the growth rate of the vapor bubble. So far, different computational methods have been proposed for the computation of heat and mass transfer rate during boiling. In many studies [46-48], that rate is computed by assuming a temperature difference between the liquid-vapor interface and a saturation temperature; the calculation depends on an empirically derived accommodation coefficient though. A different approach is to compute the temperature gradients at the center or faces of the interface cells [49, 50]. The precise location of the interface is ignored, making these methods computationally inexpensive but not very accurate.

The employed method in the current study computes the temperature gradient at the liquid-vapor interface with the temperature of only one computational cell in the liquid side, implying that the temperature of the vapor phase is uniform and equal to the saturation temperature T_{sat}. The interface temperature is also fixed at the saturation point T_{sat}, since the growth is controlled by heat diffusion, while the mass transfer rate (kg/s) is related to the local temperature gradient. Another significant feature of the algorithm is that it introduces a source term in the energy equation, in order to impose an accurate temperature value at the interface cells. This approach assumes that the temperature profile across the interface region is linear, which can be considered as a reasonable assumption as long as the grid is dense. More details about the OCASIMAT algorithm are provided in [43].

3. Results and discussion

To the best of our knowledge, suitable data from single emulsion droplet experiments in engine thermodynamic conditions are not available for a direct comparison with the results of the current CFD model. To compare against the experimental results of [51], the simulation of several water sub-droplets is required. This is prohibited since it requires a 3D computational domain with several micro-droplets randomly distributed inside the host droplet that would dramatically increase the computation cost. However, since homogeneous boiling occurs in puffing/micro-explosions, simulation of a simplified configuration has been performed in order to examine if the developed numerical model is capable of reproducing such a phenomenon. The results are compared against an analytical solution.

3.1 Spherical bubble growth inside an infinite water pool (Homogeneous boiling)

3.1.1 Computational setup and model validation

Vapor bubble growth inside a superheated liquid pool is investigated using the aforementioned CFD model, while the OCASIMAT algorithm has been implemented for the estimation of mass transfer rate. The latter directly depends on the nondimensional Stefan number ($St = c_{pl} \Delta T_s / h_{lv}$). The flow equations are solved in an axisymmetric domain, where in the left vertical axis, symmetry boundary condition is imposed. All the rest boundaries are open, where velocity 1st gradient is set to zero (Figure 3).

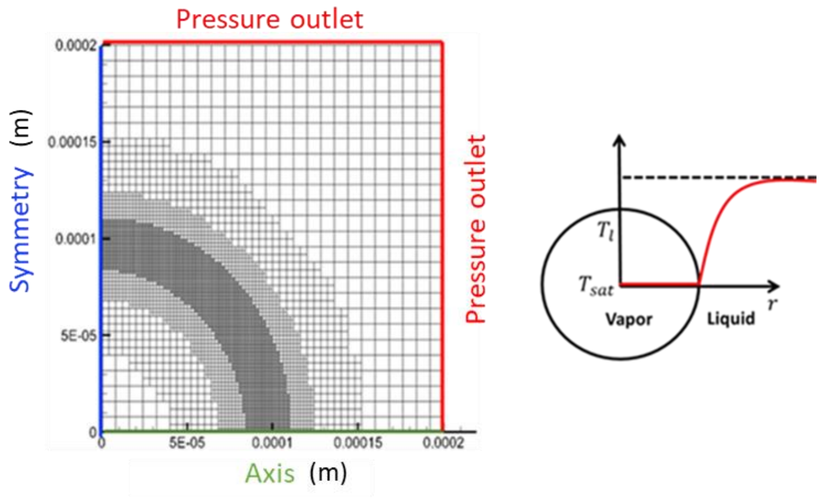

Figure 3. Computational mesh refined locally alongside with boundary conditions (Left panel). Schematic illustration of thermal boundary layer (Right panel).

The domain extents up to a distance of $2R_0$ in both vertical and horizontal directions; the same configuration has been employed in past studies [43, 47, 49, 52]. In order to save computational cost, an adaptive local refinement method has been employed [53]. From the Mikic relationship [32], it was computed that the transition to the diffusion controlled growth, in the current case, occurs when the bubble radius is equal to 6 μm. Here, the simulation starts from an initial bubble radius R_0 equal to 100 μm, where heat diffusion is already dominant and an initial thermal boundary layer (TBL) has been developed in the liquid phase. Moreover, a mesh independence study has been performed in order to retrieve the adequate mesh resolution needed for the TBL to be resolved. The results are compared against an analytical solution, which is described in the following paragraph. For the CFD model to be in agreement with analytical solution, it was found out that the base grid resolution should be 10 cpR with 4 levels of refinement, corresponding to 160 cpR at the beginning of the simulation.

The analytical solution for the case of bubble growth inside an infinite liquid is derived by [30]. The solution assumes that the bubble radius is given by the following relationship:

$$R_b = 2b\sqrt{a_w t}$$

$$b = \sqrt{\frac{3}{\pi}}\left\{\frac{\Delta T_s}{\left(\frac{\rho_g}{\rho_w}\right)\left[\frac{h_{lv}}{c_{p,w}} + \left(\frac{c_{p,w} - c_{p,g}}{c_{p,w}}\right)\Delta T_s\right]}\right\} \tag{10}$$

Here, b is a dimensionless bubble growth constant where its value depends on the superheat degree (ΔT_s) and the thermophysical properties of the material examined. The vapor bubble, with fluid properties corresponding to that of water at atmospheric conditions, is growing inside a temperature field with superheat degree of 5 K ($St = c_{p,w}\Delta T_s/h_{lv} = 0.01$). Results in the left panel of Figure 4 clearly indicate that the accuracy of the simulation improves with smaller mesh size. Specifically, for mesh size equal to 1 μm (blue solid line), where the initial thickness of the thermal boundary layer (TBL) is computed equal to 12 μm, it is observed that the model results are in perfect agreement with that of the theoretical solution. Next, a number of parametric cases was performed, in order to examine the model performance for different values of St and density ratios. In order to estimate the deviation of the CFD model from theory, a bubble growth constant (b_{CFD}) was derived for each parametric case and compared against the corresponding constant b of the analytical solution. The nondimensional error is expressed as $b - b_{CFD}/b_{CFD}$ and it seems significant for high Stefan numbers. The error decreases up to a point where mesh resolution becomes higher. In general, the emulsion droplets are examined for conditions where density ratio is low, due to high pressure (black rectangular shape); in this range of density ratio and for St up to 0.03, the computed error is not significant.

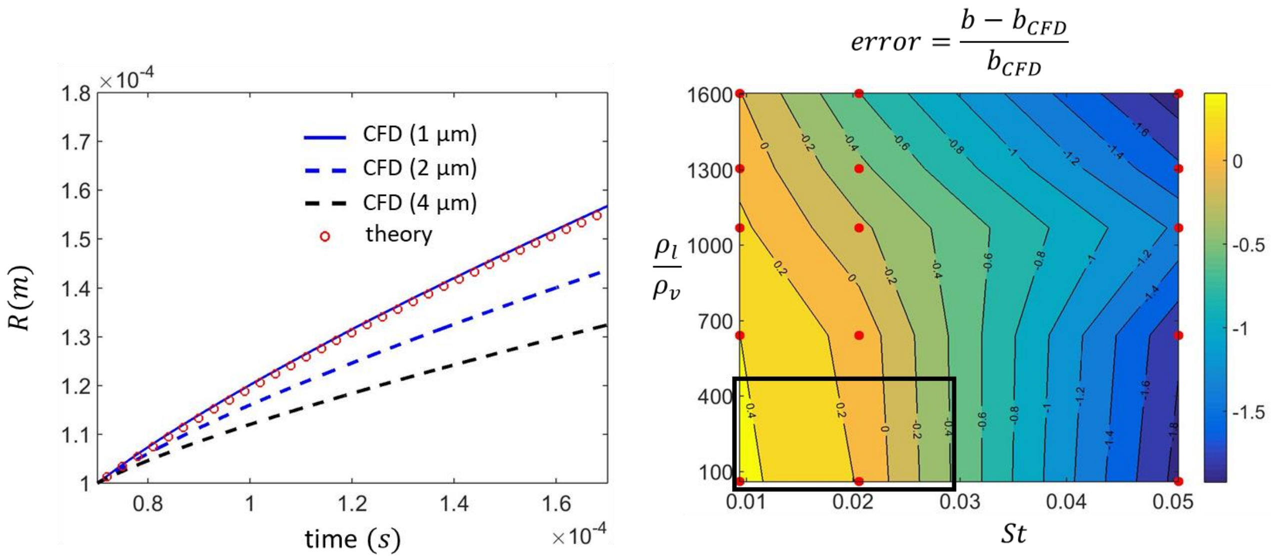

Figure 4. Prediction of the bubble growth rate for different grid resolutions (Left panel). Map indicating the error between the predictions of CFD and analytical solution (Right panel)

3.2 Emulsion breakup subjected to aerodynamic forces

3.2.1 Computational setup and examined cases

The initial conditions in the numerical domain reflect typical conditions of a HFO droplet inside the combustion chamber of marine Diesel engines [54]. Equations are solved in an axisymmetric domain where the left vertical axis is a velocity inlet boundary that imposes the velocity of the stream flow, while the rest boundaries are open (i.e. velocity gradient is set to zero). The domain extents up to a distance of $5D_d$ in the vertical direction and $10D_d$ in the horizontal one (Figure 5). Initially, 2 VoF equations are solved with an implicit VOF solver, while an additional VoF equation is solved after vapor is formed. For the spatial discretization of VoF equation, the Compressive scheme is used [55], while momentum equation is spatially discretized with a second order scheme, where quantities at cell faces are computed using a multidimensional linear reconstruction approach [56]. The energy equation is spatially discretised with a first order upwind scheme. The local grid refinement technique [53] enhances the accuracy of the computations at the interface region, while achieving low computational cost compared to a simulation with a uniform grid of the same density. Base grid resolution is such that, with 6 levels of refinement, the initial vapor bubble resolution is ∽2 cpR, while the resolution corresponding to the outer droplet is 200 cpR.

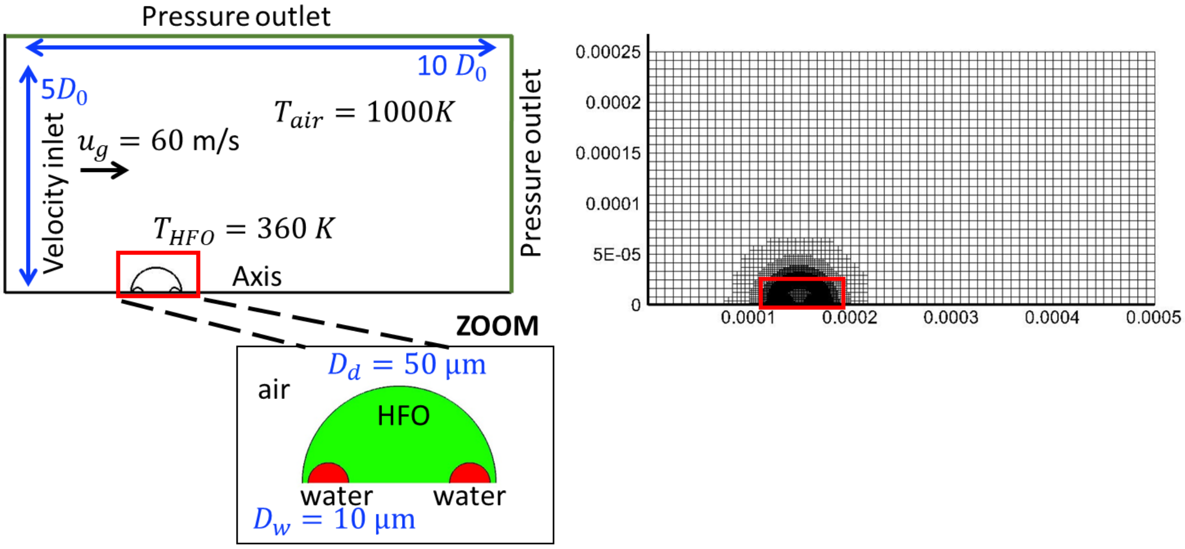

Figure 5. Computational axisymmetric domain, with zoom at levels of local refinement around the HFO-air and HFO-water interfaces.

In all examined cases, the W/HFO emulsion droplet contains two water sub-droplets which are located in the front and the back of the oil droplet, in order to capture the interface rupturing; this may occur in both sides depending on the local temperature. The emulsion droplet is placed at ambient pressure $p = 30$ bar and temperature $T_g = 1000$ K. The droplet's injection temperature is 360 K while the boiling temperatures of HFO and water are 660 K and 506 K, respectively. The physical properties of HFO are representative of those used in marine engines. Liquid density, dynamic viscosity and surface tension can be found in the work of [57], while thermal conductivity and heat capacity are computed by empirical relationships provided by [58]; these were assumed constant without any temperature dependence. The initial HFO droplet diameter is $D_{HFO} = 50$ μm, which is typical droplet size in sprays [59], while the diameter of the embedded water droplets was selected equal to $D_w = 10$ μm. That size has been also investigated in past studies [15, 60, 61]. At this point, it should be mentioned that it's rather complicated to relate the sub-droplet size with the corresponding water content of the emulsion, since emulsions may contain different amount of water sub-droplets but the same water content; in both cases it is expected a different puffing/micro-explosion outcome. The superheat degree, which is an input parameter to the model, has been selected equal to $\Delta T_s = 10$. The latter value corresponds to a St equal to 0.02. For the aforementioned St and the computed water-water vapor density ratio ($\rho_w/\rho_v = 60$), the OCASIMAT algorithm predicts with high accuracy the bubble growth rate; according to Figure 4, the error is less than 0.2. The examined Weber numbers in the cases range from 40 to 190, which correspond to droplet velocities in the range of 10-100 m/s. The latter is a typical velocity range in HFO fueled engines [59]. The Ohnesorge number is calculated equal to 0.9, implying that viscous phenomena are important. The thermophysical properties and nondimensional numbers are summarized in the following tables.

	Units	Water		HFO	Air
		Liquid	Vapor		
$\boldsymbol{T}$	K	360	506	360	1000
$\boldsymbol{\rho}$	kg m^{-3}	968	15	907	10.3
$\boldsymbol{c_p}$	J kg^{-1} K^{-1}	4195	3612	2020	1143
$\boldsymbol{\kappa}$	W m^{-1} K^{-1}	0.675	0.047	0.127	0.068
$\boldsymbol{\mu}$	kg m^{-1} s^{-1}	3.2 10^{-4}	1.69 10^{-5}	0.032	4.3 10^{-5}
$\boldsymbol{h_{lv}}$	J kg^{-1}	1.794 10^{6}			

Table 1. Thermophysical properties (computed by [58]). The pressure was assumed constant at 30bar.

$\boldsymbol{We_g}$	$\rho_g u_{rel}^2 D_{HFO}/\sigma$	70
$\boldsymbol{Pe_{HFO}}$	$D_{HFO} u_{oil}/a_{oil}$	200
$\boldsymbol{Re_g}$	$\rho_g D_{HFO} u_{rel}/\mu_g$	720
$\boldsymbol{Oh_{HFO}}$	$\mu_{HFO}/\sqrt{\rho_{HFO}\sigma D_{HFO}}$	0.9
$\boldsymbol{St_w}$	$c_{pl,w}\Delta T_s/h_{lv}$	2.3 10^{-2}

Table 2. Nondimensional numbers

3.2.2 W/HFO emulsion droplet breakup

Here, W/HFO emulsion droplet breakup is examined for a reference case where the initial velocity of the air stream is $u_g = 60$ m/s, corresponding to $Weber\ number\ We$=70. The temporal evolution of the emulsion droplet is illustrated in Figure 6. The upper part shows the temperature field alongside with the streamlines, while in the lower part the contributing phases are illustrated. The time (t^*) is non-dimensionalised with the shear timescale t_{sh}. One can see that at the initial stage, steep temperature gradients are formed near the droplet interface. At $t^* = 0.06$, a temperature distribution is formed in the surrounding gas phase; the emulsion droplet is subjected to convective heating and the inner temperature profile tends to follow the streamlines; the inner droplet temperature has not increased much though. At the next time instance ($t^* = 0.64$), the same features in the gas phase are observed but the temperature of the front water sub-droplet has locally reached the superheat degree for the onset of bubble formation. As the criteria for the vapor generation have been fulfilled, the appearance of a vapor bubble is observed. The vapor bubble starts growing due to the temperature difference at its interface. The growth rate of the bubble formed in the upstream droplet is shown in Figure 7 in terms of the dimensionless equivalent bubble radius (this was obtained from the bubble volume). In the horizontal axis, the time instance of bubble formation has shifted to zero. As seen, the bubble radius grows in time according to $\sqrt{t}$, while the growth constant b found to be higher compared to the theoretical prediction. That deviation from theory is expected, since a number of assumptions is violated, i.e. bubble grows inside a droplet instead of an infinite pool, spherical asymmetry, shape deformation and bubble motion. Fragmentation of the HFO-air boundary occurs at $t^* = 1.01$ and water vapor is escaping in the ambient air; in the present work, this time instant is considered as the breakup initiation time. This feature is observed clearly at $t^* = 1.12$ (vapor phase indicated by red colour). The corresponding vapor bubble growth and breakup process occurs also, with a temporal delay, in the downstream region of the parent droplet. These results indicate that the breakup regime in this case is puffing, since partial breakup of the W/HFO droplet occurs. Finally, it has to be noted that the droplet deformation due to aerodynamic forces plays a minor role here, since the combination of We and Oh examined corresponds to a relative slow deformation process.

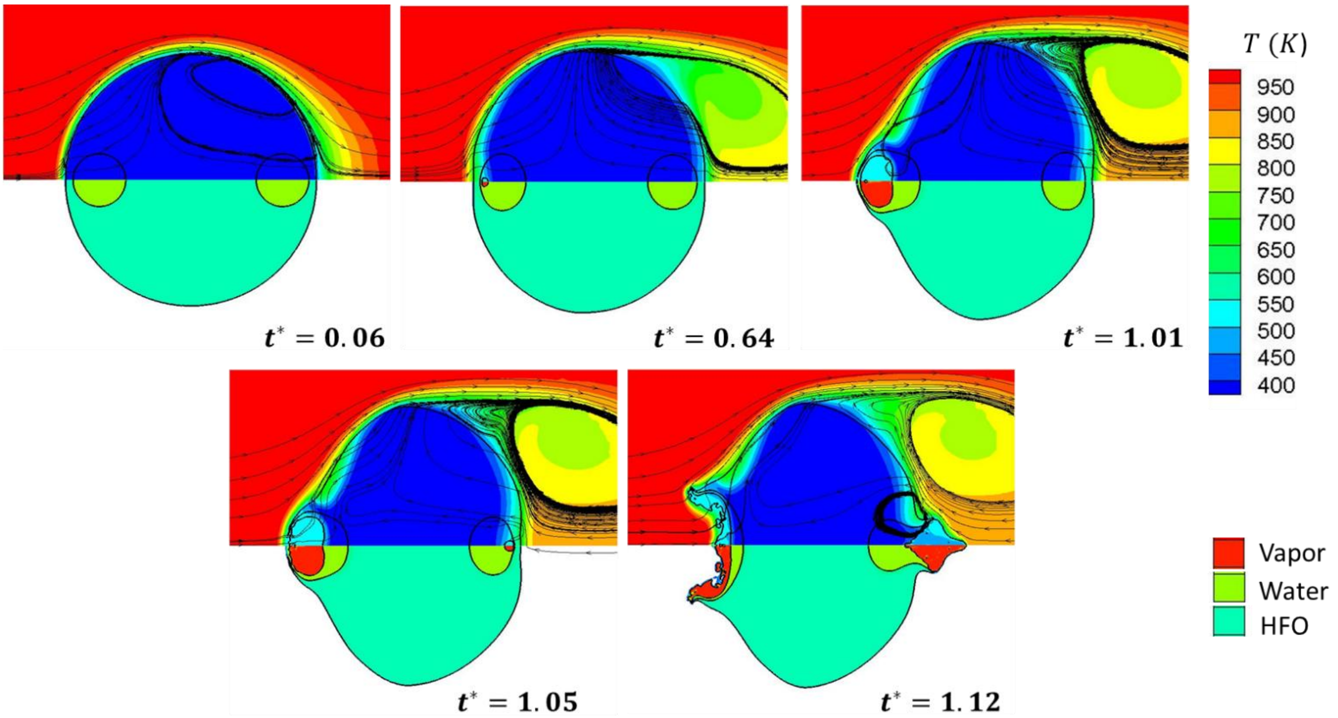

Figure 6. Temporal evolution of emulsion droplet breakup. Upper part: Temperature profile. Lower part: HFO, Water liquid and Water vapor phases indicated by ciel, green and red respectively.

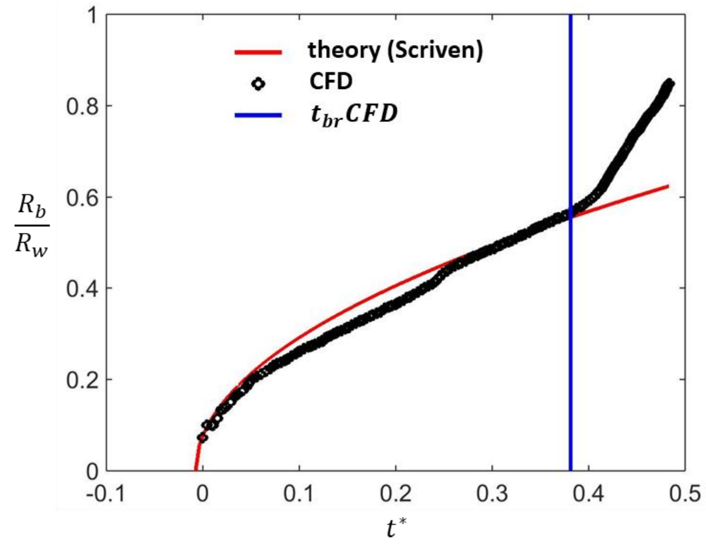

Figure 7. Nondimensional vapor bubble radius predicted by Scriven solution (red solid line) and CFD simulation (black scatter symbols) for the front bubble with $We = 70$ and a corresponding breakup initiation time (vertical blue line)

3.2.3 Parametric study with Weber number

Having identified the physical phenomena occurring during the coupled thermal and aerodynamic loading of the droplet, the effect of We on the breakup initiation time of the W/HFO emulsion droplet is examined in detail. For the examined range of We, simulations are also performed for neat HFO droplets in order to predict their breakup initiation time due to aerodynamic forces and compare it against those when puffing/micro-explosion is accounted for. For the default Weber number case ($We = 70$), the temporal evolution of the neat HFO droplet (lower panel) is illustrated in Figure 8, alongside with those of the benchmark W/HFO emulsion cases (upper panel). The neat HFO droplet breaks under aerodynamic forces at $t^* = 10.5$, which is an order of magnitude longer compared to the breakup initiation time of W/HFO emulsion. This clearly reveals the droplet fragmentation acceleration when using emulsified droplets in viscous fuels.

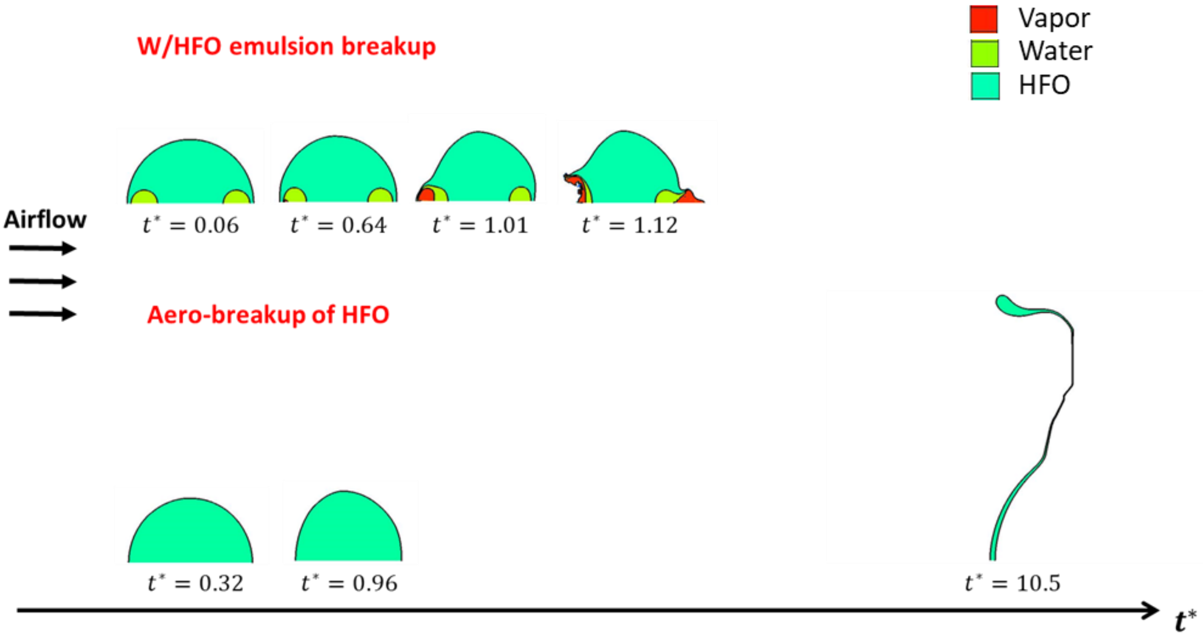

Figure 8. Temporal evolution of W/HFO emulsion droplet (Upper panel) and neat HFO droplet (Lower panel) for We number equal to 70.

In the left panel of Figure 9, the dependence of the breakup initiation time on the We is illustrated. For the case of aerodynamic droplet breakup (blue scatter symbols), the breakup initiation time decreases strongly with increasing We, which is in accordance with several past studies [54, 62-69]. Regarding the breakup of emulsified droplets (black scatter symbols), the right-hand side panel of Figure 9 shows a weakly decreasing dependence on We. In each We correspond two black scatters, which stand for breakup initiation time of the upstream and downstream side of the droplet emulsion. It is observed that the difference between the two time instances decreases as We increases. Overall, it is important to mention that the emulsion breakup occurs 4-10 times faster than the aerodynamic breakup. The latter trend indicates that puffing/micro-explosion process can speed up the breakup of the droplet relative to the mechanism of the aerodynamic breakup for the range of conditions ($Oh \approx 1, We < 200$) examined here.

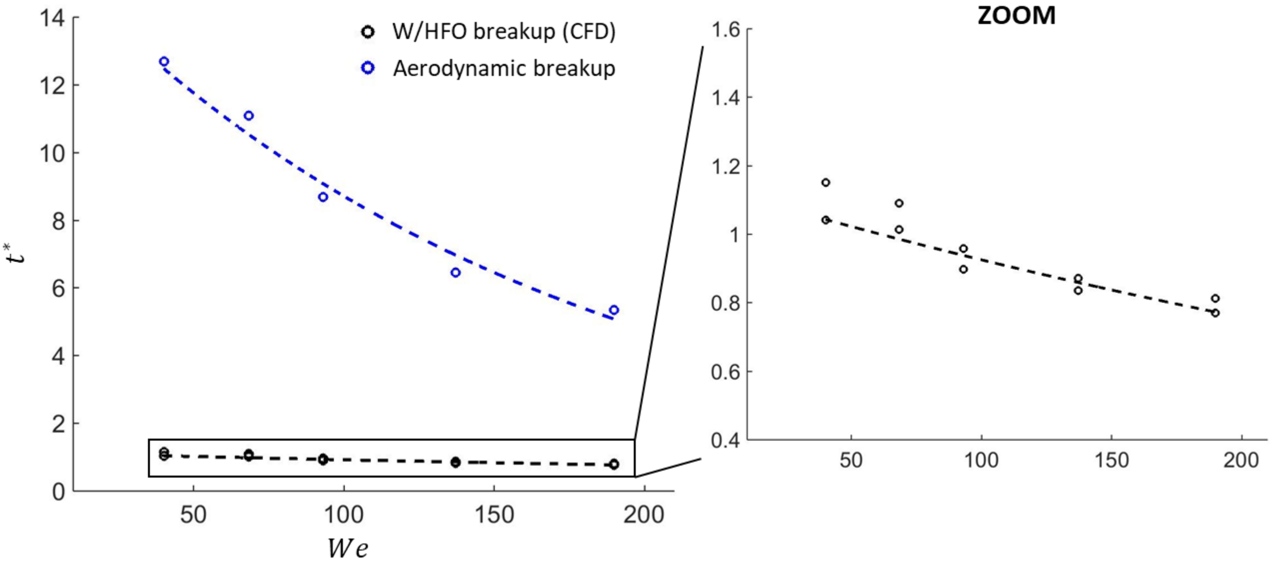

Figure 9. Breakup time of W/HFO emulsion droplet for a range of We (black scatter symbols). Aerodynamic breakup of neat HFO droplet for the corresponding range of We (blue solid line).

3.2.4 Droplet deformation

In the previously presented Figure 6, it was observed that the W/HFO emulsion droplet was slightly deformed after its breakup initiation time compared to its initial spherical shape. It is expected that if a larger amount of water sub-droplets is present in the parent droplet, simultaneous (and/or successive) boiling will occur in each sub-droplet and the induced deformation will be accelerated. This process is indicated in Figure 10, where the dimensionless surface area of the W/HFO emulsion droplet and the neat HFO droplet are illustrated; the surface area of the latter has significantly increased up to the breakup initiation time. It is clear that the surface area of the W/HFO emulsion increases during the successive explosion events caused by the downstream and upstream water sub-droplet.

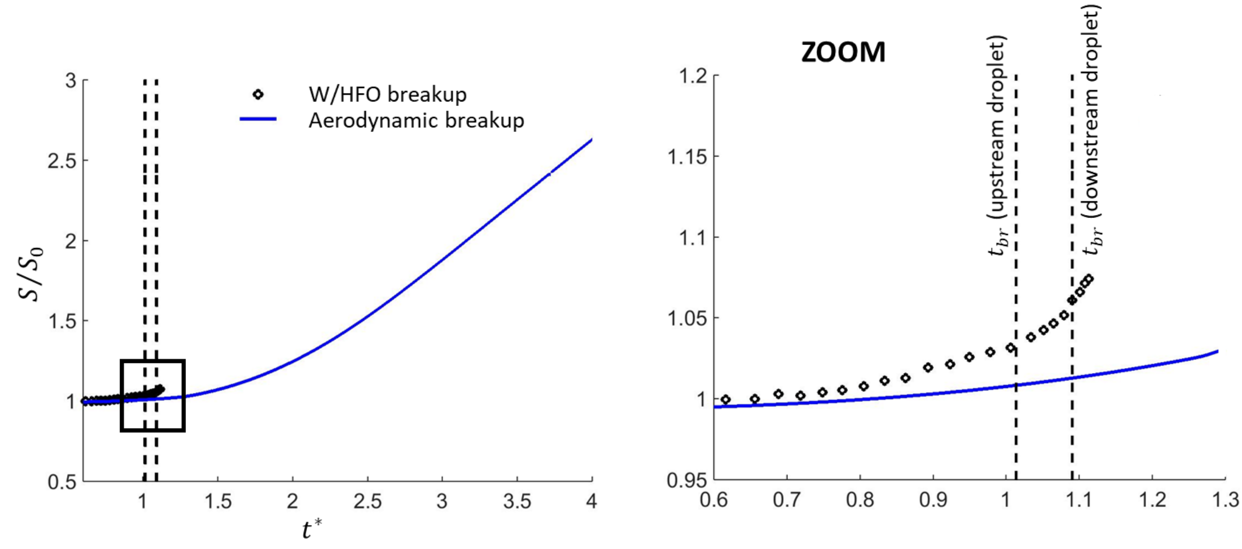

Figure 10. Temporal evolution of the dimensionless surface area of the W/HFO emulsion (scatter symbols) and the neat HFO droplet (blue line)

4. Conclusions

The heating and interface dynamics leading to fragmentation of immiscible heavy fuel oil-water droplets, termed as W/HFO emulsions, was examined numerically by solving the incompressible Navier-Stokes and energy conservation equations alongside with three sets of VoF transport equations utilised for resolving the interfaces between the co-existing HFO, water liquid and water vapour. A key feature of the puffing/micro-explosion phenomenon is the explosive boiling of embedded water droplets. To resolved this, an algorithm predicting the nucleation water vapour at a certain superheat degree, typical for water-HFO interfaces, was utilised. This algorithm scans the temperature field of liquid water and forms a vapor bubble with pre-defined properties. The subsequent vaporization rate of the growing bubbles inside the water sub-droplet, was computed with the OCASIMAT algorithm. The latter was validated for the idealised configuration of a vapor bubble growing inside an infinite superheated liquid pool, against a theoretical solution. Next, numerical simulations of W/HFO emulsion droplet breakup were performed. A benchmark case was presented for a W/HFO emulsion droplet with an initial velocity $u_g = 60$ m/s, at ambient pressure $p = 30$ bar and temperature $T_g = 1000$ K. Two water sub-droplets were initialised inside the parent HFO liquid droplet, downstream and upstream relative to the surrounding air flow motion. It was observed that the atomization of the emulsion droplet is puffing-induced. Next, the model was used to perform numerical simulations of W/HFO emulsion droplet breakup for a range of We that are representative for Diesel engines. The diameter of HFO droplet and Oh (50 μm and 0.9, respectively) were kept unchanged for all parametric cases investigated. Predictions from those simulations have been compared with those corresponding to cases of aerodynamic breakup of neat HFO droplets having identical properties and initial conditions as those of the corresponding emulsions. It was revealed that for the viscous fuel examined (Oh>1) puffing/micro-explosion speeds up the droplet breakup by almost an order of magnitude relative to the aerodynamic breakup. This was more evident for relatively low We, while increasing the We resulted in faster droplet breakup.

Acknowledgement

Financial support from the MSCA-ITN-ETN of the European Union's H2020 programme, under REA grant agreement n. 675676 is acknowledged.

Appendix A. Effect of bubble surface depth and superheat degree on W/HFO emulsion breakup

In subsection 2.2 a mechanistic model that is responsible for bubble formation inside the embedded water sub-droplet was presented. The criteria under which a vapor bubble is generated in a computational cell, are that the latter should reach a superheat degree (ΔT_s) and have a specific distance (d_i) from the water-HFO interface. Both are input parameters of the model. A parametric study with d_i and ΔT_s is performed, for the reference case of $We = 70$, in order to investigate their sensitivity on emulsion breakup time. The results are compared against the parametric study of breakup time with We (Figure 9). Horizontal axis of Figure 11 indicates the aforementioned parameters $\lambda =< d_i, \Delta T_s, We >$, which are normalised with the examined values of the reference case. Results show that breakup initiation time slightly increases with d_i (blue scatter symbols); this is expected since it takes some time for heat transfer to accur deeper inside the water sub-droplet and result to subsequently formation of the water vapour bubble. Regarding the effect of superheat degree, it seems that breakup initiation time slightly changes (red scatter symbols) without having a clear trend with ΔT_s. Finally, it is observed that both parameters are much less sensitive to breakup initiation time compared to the effect of We (black scatter symbols); when the latter increases five times, the breakup initiation time becomes approximately an order of magnitude lower.

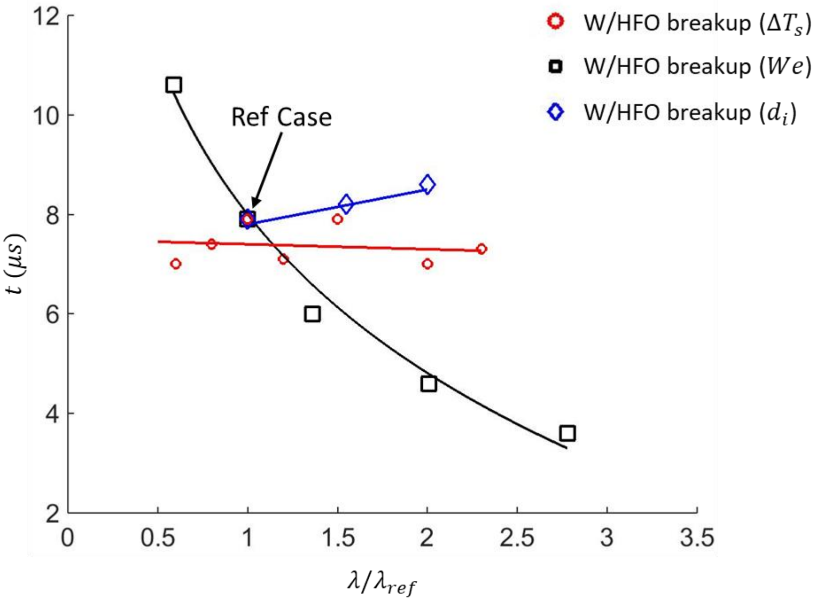

Figure 11. Breakup initiation time of W/HFO emulsion with superheat degree (red scatter symbols), bubble surface depth (blue scatter symbols) and We (black scatter symbols)

References

1. Reitz, R., et al., *IJER editorial: the future of the internal combustion engine*. 2020, SAGE Publications Sage UK: London, England.
2. The Outlook for Energy: A View to 2040. Exxon Mobil Corporation, 2019.
3. Kolev, N.I., *Forced convection boiling*, in *Multiphase Flow Dynamics 3: Thermal Interactions*, N.I. Kolev, Editor. 2012, Springer Berlin Heidelberg. p. 213-243.

4. Kumar, M.S., J. Bellettre, and M. Tazerout, *The use of biofuel emulsions as fuel for diesel engines: a review*. 2009, SAGE Publications Sage UK: London, England.

5. Qin, D., et al., *IPCC, 2007: Summary for Policymakers.* 2007.

6. Jegannathan, K.R., et al., *Production of biodiesel using immobilized lipase—a critical review.* Critical Reviews in Biotechnology, 2008. **28**(4): p. 253-264.

7. Tan, T., et al., *Biodiesel production with immobilized lipase: a review.* Biotechnology advances, 2010. **28**(5): p. 628-634.

8. Tarlet, D., et al., *Formulation and combustion of emulsified fuel: The changes in emission of carbonaceous residue.* International journal of energy research, 2010. **34**(8): p. 688-694.

9. Bedford, F., et al., *Effects of direct water injection on DI diesel engine combustion*. 2000, SAE Technical Paper.

10. Tauzia, X., A. Maiboom, and S.R. Shah, *Experimental study of inlet manifold water injection on combustion and emissions of an automotive direct injection diesel engine.* Energy, 2010. **35**(9): p. 3628-3639.

11. Basha, J.S. and R. Anand, *An experimental study in a CI engine using nanoadditive blended water–diesel emulsion fuel.* International journal of green energy, 2011. **8**(3): p. 332-348.

12. Kadota, T. and H. Yamasaki, *Recent advances in the combustion of water fuel emulsion.* Progress in energy and combustion science, 2002. **28**(5): p. 385-404.

13. Kumar, M.S., J. Bellettre, and M. Tazerout, *Investigations on a CI engine using animal fat and its emulsions with water and methanol as fuel*. 2005, SAE Technical Paper.

14. Avedisian, C. and R. Andres, *Bubble nucleation in superheated liquid—liquid emulsions.* Journal of colloid and interface science, 1978. **64**(3): p. 438-453.

15. Shinjo, J., et al., *Physics of puffing and microexplosion of emulsion fuel droplets.* Physics of Fluids (1994-present), 2014. **26**(10): p. 103302.

16. Shinjo, J., et al., *Modeling temperature distribution inside an emulsion fuel droplet under convective heating: a key to predicting microexplosion and puffing.* Atomization and Sprays, 2016. **26**(6).

17. Shepherd, J.E. and B. Sturtevant, *Rapid evaporation at the superheat limit.* Journal of Fluid Mechanics, 2006. **121**: p. 379-402.

18. Frost, D., *Dynamics of explosive boiling of a droplet.* The Physics of fluids, 1988. **31**(9): p. 2554-2561.

19. Ochoterena, R., et al., *Optical studies of spray development and combustion of water-in-diesel emulsion and microemulsion fuels.* Fuel, 2010. **89**(1): p. 122-132.

20. Park, S., et al., *The characteristic of spray using diesel water emulsified fuel in a diesel engine.* Applied energy, 2016. **176**: p. 209-220.

21. Zhu, M., et al., *An experimental investigation into the ignition and combustion characteristics of single droplets of biochar water slurry fuels in air.* Applied energy, 2017. **185**: p. 2160-2167.

22. Califano, V., R. Calabria, and P. Massoli, *Experimental evaluation of the effect of emulsion stability on micro-explosion phenomena for water-in-oil emulsions.* Fuel, 2014. **117**: p. 87-94.

23. Mura, E., et al., *Study of the micro-explosion temperature of water in oil emulsion droplets during the Leidenfrost effect.* Experimental Thermal and Fluid Science, 2012. **43**: p. 63-70.

24. Fuchihata, M., T. Ida, and Y. Mizutani, *Observation of microexplosions in spray flames of light oil water emulsions. II. Influence of temporal and spatial resolution in high speed videography.* Nippon Kikai Gakkai

Ronbunshu B Hen(Transactions of the Japan Society of Mechanical Engineers Part B)(Japan), 2003. **15**(6): p. 1503-1508.

25. Watanabe, H. and K. Okazaki, *Visualization of secondary atomization in emulsified-fuel spray flow by shadow imaging.* Proceedings of the Combustion Institute, 2013. **34**(1): p. 1651-1658.

26. Brennen, C.E., *Cavitation and bubble dynamics*. 2014: Cambridge University Press.

27. Rayleigh, L., *VIII. On the pressure developed in a liquid during the collapse of a spherical cavity.* The London, Edinburgh, and Dublin Philosophical Magazine and Journal of Science, 1917. **34**(200): p. 94-98.

28. Forster, H. and N. Zuber, *Dynamics of vapor bubbles and boiling heat transfer.* AIChE Journal, 1955. **1**(4): p. 531-535.

29. Plesset, M. and S.A. Zwick, *The growth of vapor bubbles in superheated liquids.* Journal of Applied Physics, 1954. **25**(4): p. 493-500.

30. Scriven, L., *On the dynamics of phase growth.* Chemical engineering science, 1959. **10**(1-2): p. 1-13.

31. Van Stralen, S., *The growth rate of vapour bubbles in superheated pure liquids and binary mixtures: Part I: Theory.* International Journal of Heat and Mass Transfer, 1968. **11**(10): p. 1467-1489.

32. Mikic, B., W. Rohsenow, and P. Griffith, *On bubble growth rates.* International Journal of Heat and Mass Transfer, 1970. **13**(4): p. 657-666.

33. Shusser, M. and D. Weihs, *Explosive boiling of a liquid droplet.* International journal of multiphase flow, 1999. **25**(8): p. 1561-1573.

34. Zeng, Y. and F.L. Chia-fon, *Modeling droplet breakup processes under micro-explosion conditions.* Proceedings of the Combustion Institute, 2007. **31**(2): p. 2185-2193.

35. Girin, O.G., *Dynamics of the emulsified fuel drop microexplosion.* Atomization and Sprays, 2017. **27**(5).

36. Sazhin, S., et al., *A simple model for puffing/micro-explosions in water-fuel emulsion droplets.* International Journal of Heat and Mass Transfer, 2019. **131**: p. 815-821.

37. Guildenbecher, D., C. López-Rivera, and P. Sojka, *Secondary atomization.* Experiments in Fluids, 2009. **46**(3): p. 371.

38. Nicholls, J. and A. Ranger, *Aerodynamic shattering of liquid drops.* Aiaa Journal, 1969. **7**(2): p. 285-290.

39. Nissar, Z., et al., *A model for puffing/microexplosions in water/fuel emulsion droplets.* International Journal of Heat and Mass Transfer, 2020. **149**: p. 119208.

40. Zhang, Y., et al., *A new puffing model for a droplet of butanol-hexadecane blends.* Applied Thermal Engineering, 2018. **133**: p. 633-644.

41. Avedisian, C. and I. Glassman, *Superheating and boiling of water in hydrocarbons at high pressures.* International Journal of Heat and Mass Transfer, 1981. **24**(4): p. 695-706.

42. Avedisian, C.T., *The homogeneous nucleation limits of liquids.* Journal of physical and chemical reference data, 1985. **14**(3): p. 695-729.

43. Perez-Raya, I. and S.G. Kandlikar, *Discretization and implementation of a sharp interface model for interfacial heat and mass transfer during bubble growth.* International Journal of Heat and Mass Transfer, 2018. **116**: p. 30-49.

44. Hirt, C.W. and B.D. Nichols, *Volume of fluid (VOF) method for the dynamics of free boundaries.* Journal of Computational Physics, 1981. **39**(1): p. 201-225.

45. Brackbill, J., D.B. Kothe, and C. Zemach, *A continuum method for modeling surface tension.* Journal of computational physics, 1992. **100**(2): p. 335-354.

46. Kunkelmann, C. and P. Stephan, *CFD simulation of boiling flows using the volume-of-fluid method within OpenFOAM.* Numerical Heat Transfer, Part A: Applications, 2009. **56**(8): p. 631-646.

47. Magnini, M., B. Pulvirenti, and J.R. Thome, *Numerical investigation of hydrodynamics and heat transfer of elongated bubbles during flow boiling in a microchannel.* International Journal of Heat and Mass Transfer, 2013. **59**: p. 451-471.

48. Maki, K.L. and S. Kumar, *Fast evaporation of spreading droplets of colloidal suspensions.* Langmuir, 2011. **27**(18): p. 11347-11363.

49. Sato, Y. and B. Ničeno, *A sharp-interface phase change model for a mass-conservative interface tracking method.* Journal of Computational Physics, 2013. **249**: p. 127-161.

50. Sun, D., J. Xu, and Q. Chen, *Modeling of the evaporation and condensation phase-change problems with FLUENT.* Numerical Heat Transfer, Part B: Fundamentals, 2014. **66**(4): p. 326-342.

51. Moussa, O., et al., *INSIGHT OF AWATER-IN-OIL EMULSION DROP UNDER LEIDENFROST HEATING USING LASER-INDUCED FLUORESCENCE OPTICAL DIAGNOSTICS.* Atomization and Sprays, 2019. **29**(1).

52. Tanguy, S., et al., *Benchmarks and numerical methods for the simulation of boiling flows.* Journal of Computational Physics, 2014. **264**: p. 1-22.

53. Malgarinos, I., N. Nikolopoulos, and M. Gavaises, *Coupling a local adaptive grid refinement technique with an interface sharpening scheme for the simulation of two-phase flow and free-surface flows using VOF methodology.* Journal of Computational Physics, 2015. **300**: p. 732-753.

54. Stefanitsis, D., et al., *Numerical investigation of the aerodynamic breakup of Diesel and heavy fuel oil droplets.* International Journal of Heat and Fluid Flow, 2017. **68**: p. 203-215.

55. Ubbink, O. and R. Issa, *A method for capturing sharp fluid interfaces on arbitrary meshes.* Journal of Computational Physics, 1999. **153**(1): p. 26-50.

56. Barth, T. and D. Jespersen. *The design and application of upwind schemes on unstructured meshes*. in *27th Aerospace sciences meeting*. 1989.

57. Kyriakides, N., C. Chryssakis, and L. Kaiktsis, *Influence of heavy fuel properties on spray atomization for marine diesel engine applications*. 2009, SAE Technical Paper.

58. Riazi, M., *Characterization and properties of petroleum fractions*. Vol. 50. 2005: ASTM international.

59. Wadhwa, A.R., V. Magi, and J. Abraham, *Transient deformation and drag of decelerating drops in axisymmetric flows.* Physics of Fluids, 2007. **19**(11): p. 113301.

60. Khan, M.Y., et al., *A case study on the influence of selected parameters on microexplosion behavior of water in biodiesel emulsion droplets.* Journal of Energy Resources Technology, 2017. **139**(2): p. 022203.

61. Kimoto, K., Y. Owashi, and Y. Omae, *The vaporizing behavior of the fuel droplet of water-in-oil emulsion on the hot surface.* Bulletin of JSME, 1986. **29**(258): p. 4247-4255.

62. Pilch, M. and C. Erdman, *Use of breakup time data and velocity history data to predict the maximum size of stable fragments for acceleration-induced breakup of a liquid drop.* International journal of multiphase flow, 1987. **13**(6): p. 741-757.

63. Stefanitsis, D., et al., *Numerical investigation of the aerodynamic breakup of droplets in tandem.* International Journal of Multiphase Flow, 2019. **113**: p. 289-303.

64. Stefanitsis, D., et al., *Numerical investigation of the aerodynamic breakup of a parallel moving droplet cluster.* International Journal of Multiphase Flow, 2019. **121**: p. 103123.

65. Strotos, G., et al., *Non-dimensionalisation parameters for predicting the cooling effectiveness of droplets impinging on moderate temperature solid surfaces.* International Journal of Thermal Sciences, 2011. **50**(5): p. 698-711.

66. Strotos, G., et al., *Numerical investigation of aerodynamic droplet breakup in a high temperature gas environment.* Fuel, 2016. **181**: p. 450-462.

67. Strotos, G., et al., *Aerodynamic breakup of an n-decane droplet in a high temperature gas environment.* Fuel, 2016. **185**: p. 370-380.

68. Strotos, G., et al., *Predicting droplet deformation and breakup for moderate Weber numbers.* International Journal of Multiphase Flow, 2016. **85**: p. 96-109.

69. Strotos, G., et al., *Predicting the evaporation rate of stationary droplets with the VOF methodology for a wide range of ambient temperature conditions.* International Journal of Thermal Sciences, 2016. **109**: p. 253-262.